ACS OMEGA

Open Access

http://pubs.acs.org/journal/acsodf

Article

Development of a 3D Printing-Enabled Cost-Effective Multimodal Raman Probe with High Signal-to-noise Ratio Raman Spectrum Measurements

Ezekiel Edward Nettey-Oppong,[¶] Ahmed Ali,[*,¶] Jiwon Ahn, Riaz Muhammad, Hyun Jin Lee, Hyun-Woo Jeong, Kyung Min Byun,[*] and Seung Ho Choi[*]

Cite This: *ACS Omega* 2024, 9, 42822−42838

Read Online

ACCESS | Metrics & More | Article Recommendations

ABSTRACT: Raman spectroscopy has emerged as a pivotal analytical instrument, valued for its nondestructive capabilities and its capacity to provide essential material-specific insights. However, the excessive costs associated with commercially available Raman instruments present a barrier to their accessibility for many academic institutions and broader usage. Herein, we introduce an affordable and accessible approach to constructing a versatile Raman instrument capable of accommodating both spectroscopic and microscopic analyses. Through this multimodal approach that concurrently captures Raman signal and image data, we demonstrate color-based alcohol detection, showcase a high signal-to-noise ratio achieved through meticulous hardware design and signal processing, and present a cost-effective, modular design utilizing 3D printing technology. This system offers adaptability to address diverse research needs and requirements. We systematically detail the fabrication process, including the utilization of a 3D printer to produce necessary components, ultimately resulting in the assembly of a functional Raman probe system. Our experiments and subsequent analyses substantiate the accuracy and reliability of the constructed system. Specifically, we conducted experiments involving three distinct samples: water, ethanol, and methanol using the Raman probe, successfully confirming their unique Raman spectra. Furthermore, our Raman probe accurately identified ethanol concentration by assessing mixed samples with varying water-to-ethanol ratios and demonstrated a coefficient of determination value of 0.9993. This underscores the performance of the constructed Raman probe and positions it as a viable option for characterization, particularly in regions where access to conventional Raman probe may be limited.

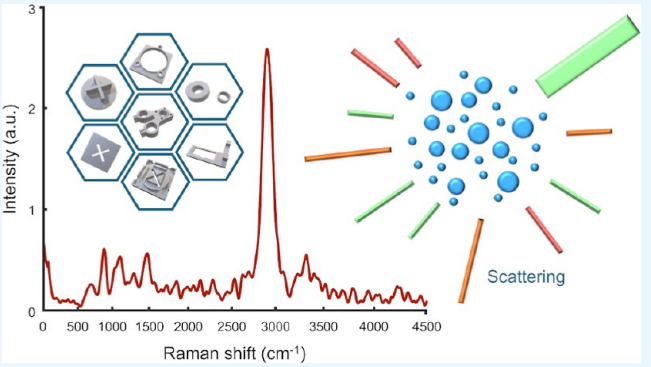

1. INTRODUCTION

Raman spectroscopy utilizes the Raman effect to gather molecular vibrational data and serves as a noninvasive method for material identification.[1] Unlike infrared (IR) spectroscopy, which is based on absorption, Raman spectroscopy relies on scattering, offering significant flexibility in sample handling and instrument design.[2,3] Due to the advancement of affordable optics, Raman spectroscopy can now be performed using portable, battery-powered devices, significantly expanding their utility for on−site activities as well as point-of-care services.[4,5] Owing to its low susceptibility to external interferences such as water, Raman spectroscopy is well-suited for the analysis of analytes in their natural environments.[6] In many domains including medical diagnostics,[7−11] pharmaceuticals,[12,13] food industries,[14] environmental quality assessment,[15] forensics,[16] homeland security,[17] anticounterfeiting measures,[18] archeology,[19] geology,[20] and the assessment of gemstone purity,[21] Raman spectroscopy has become the preferred experimental tool. It has been proven to overcome the limitations of other spectroscopic techniques.

The Raman effect denotes the phenomenon of incident photons undergoing inelastic scattering, thus, a modification in the molecular vibrational energy during light interaction.[22−24] The interaction induces transitions in molecular energy states, distinguishing the Raman effect into two categories: anti-Stokes Raman scattering and Stokes Raman scattering.[25] Concerning the initial energy, Stokes Raman scattering results in an increase in vibrational energy, while anti-Stokes Raman scattering involves a decrease. Conversely, Rayleigh scattering,

Received: May 16, 2024
Revised: September 5, 2024
Accepted: September 13, 2024
Published: September 20, 2024

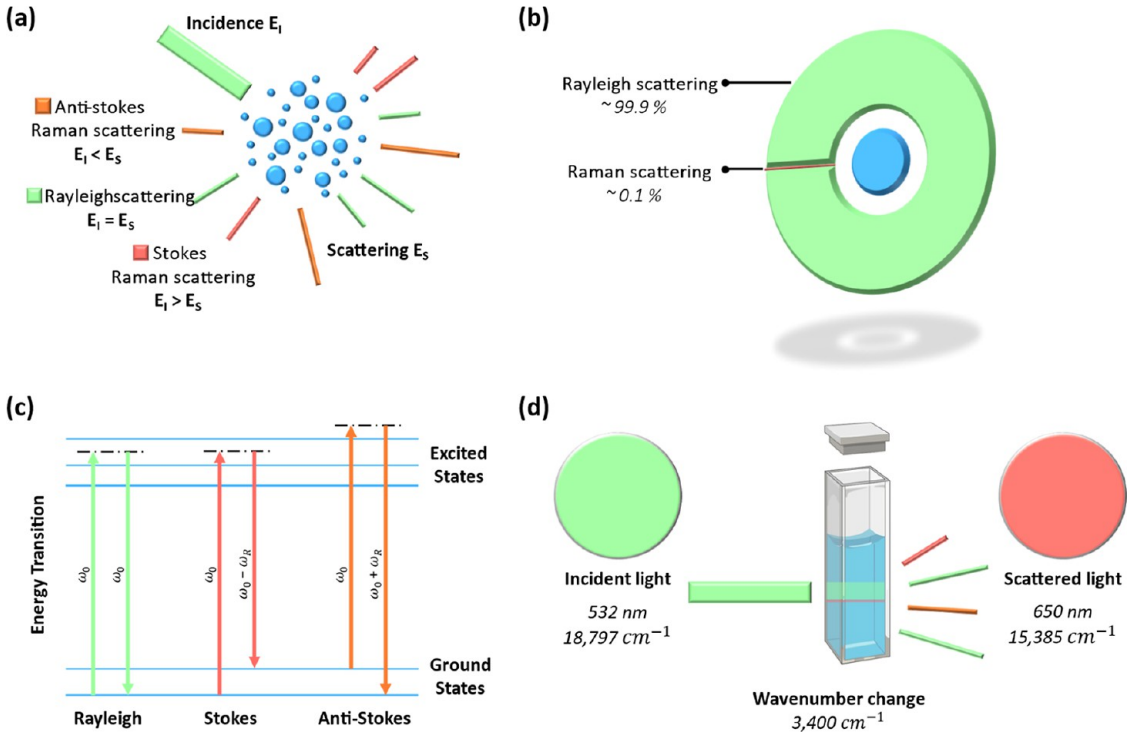

Figure 1. Raman spectroscopy principle. (a) Based on differences in vibrational energy levels, Raman scattering is classified as anti-Stokes and Stokes types. Relative to the energy of incident photons, vibrational energy remains unchanged in Rayleigh scattering, decreases in anti-Stokes scattering, and increases in Stokes scattering. (b) Elastic scattering, sometimes referred to as Rayleigh scattering, occurs when light interacts with materials and accounts for around 99.90% of photons scattered. The Raman scattering, which is an inelastic phenomenon, accounts for the other 0.10% of photons scattered. (c) An illustration of the energy exchange model involving anti-Stokes, Stokes, and Raman scattering. (d) Diagram illustrating Raman shift induced by light scattering. Notably, a wavenumber of 18,797 cm^{-1} is dispersed at 15,385 cm^{-1}. This resultant wavenumber shift of 3400 cm^{-1} arises from changes in the molecules' vibrational energy states.

depicted in Figure 1a, maintains a constant vibrational energy relative to the incident energy. Rayleigh scattering, a process in which photons are elastically scattered upon interaction with particles, accounts for nearly 99.9% of the scattered light,[26] as shown in Figure 1b. In contrast, Raman scattering, where photons are inelastically scattered upon interaction with particles, constitutes a small fraction, representing the remaining 0.1% of the scattered light.

When exposed to light, the atoms within a material undergo polarization. Subatomic particles, which carry a negative charge, become separated from atomic nuclei due to the applied electromagnetic field (EMF), resulting in the generation of an electric dipole moment. The EMF strength directly correlates with the size of the generated electric dipole moment caused by radiation exposure, and the polarizability is represented by the constant of proportionality.[24] Molecular polarizability, on the other hand, signifies the change in the distribution of surface plasmons at the molecular level in response to an applied electric field.[26] For elastic scattering, such as in Rayleigh scattering, the polarizability remains constant. Consequently, the applied EMF and the electromagnetic wave scattered possess matching frequencies. In contrast, for inelastic scattering, as observed in Raman scattering, the polarizability varies over time owing to the molecular vibrations resulting from the alterations in electron density due to nuclear movement.[24] From the Taylor expansion, the generated electric dipole moment is quantitatively represented as shown below

$$\mu = \alpha_0 E_0 \cos \omega_0 t + \frac{1}{2}\left(\frac{\partial \boldsymbol{\alpha}}{\partial \boldsymbol{q}}\right)|_{q=0} \cdot q_0 E_0 \cos(\omega_0 - \omega_R)t + \frac{1}{2}\left(\frac{\partial \boldsymbol{\alpha}}{\partial \boldsymbol{q}}\right)|_{q=0} \cdot q_0 E_0 \cos(\omega_R + \omega_0)t \quad (1)$$

where E_0 and ω_0 denote the amplitude and frequency of the incident electric field, respectively. The terms μ and ω_R correspond to the time-dependent induced electric dipole moment and the frequency of the vibrational mode, respectively. The term α_0 signifies the linear polarizability of the material, q is the nuclear displacement, where $q = 0$ designates the nuclear equilibrium position, and t represents time. Equation 1 summarizes the oscillation frequencies of the electric dipole moment, representing the scattered radiation by molecules. The first component in eq 1, representing Rayleigh scattering phenomena, has an oscillation frequency (ω_0) that is in phase with the applied EMF frequency. The second component in eq 1 displays modulated oscillation frequencies, indicating the difference between the applied EMF frequency (ω_0) and the vibrational mode (ω_R) frequency. The vibrational mode (ω_R) frequency in the second term is lower than that of the incident light, indicating that the excitation corresponds to a red shift in inelastic scattering. A relatively low frequency ($\omega_0 - \omega_R$) is produced when molecules absorb energy from the applied EMF and go through upward energy transitions, leading to this excitation. Likewise, the third component in eq 1, which represents a blue shift in inelastic scattering, illustrates de-excitation caused by an increase in frequency ($\omega_0 + \omega_R$).[27] In eq 1, the second and third components are associated with

https://doi.org/10.1021/acsomega.4c04676
ACS Omega 2024, 9, 42822−42838

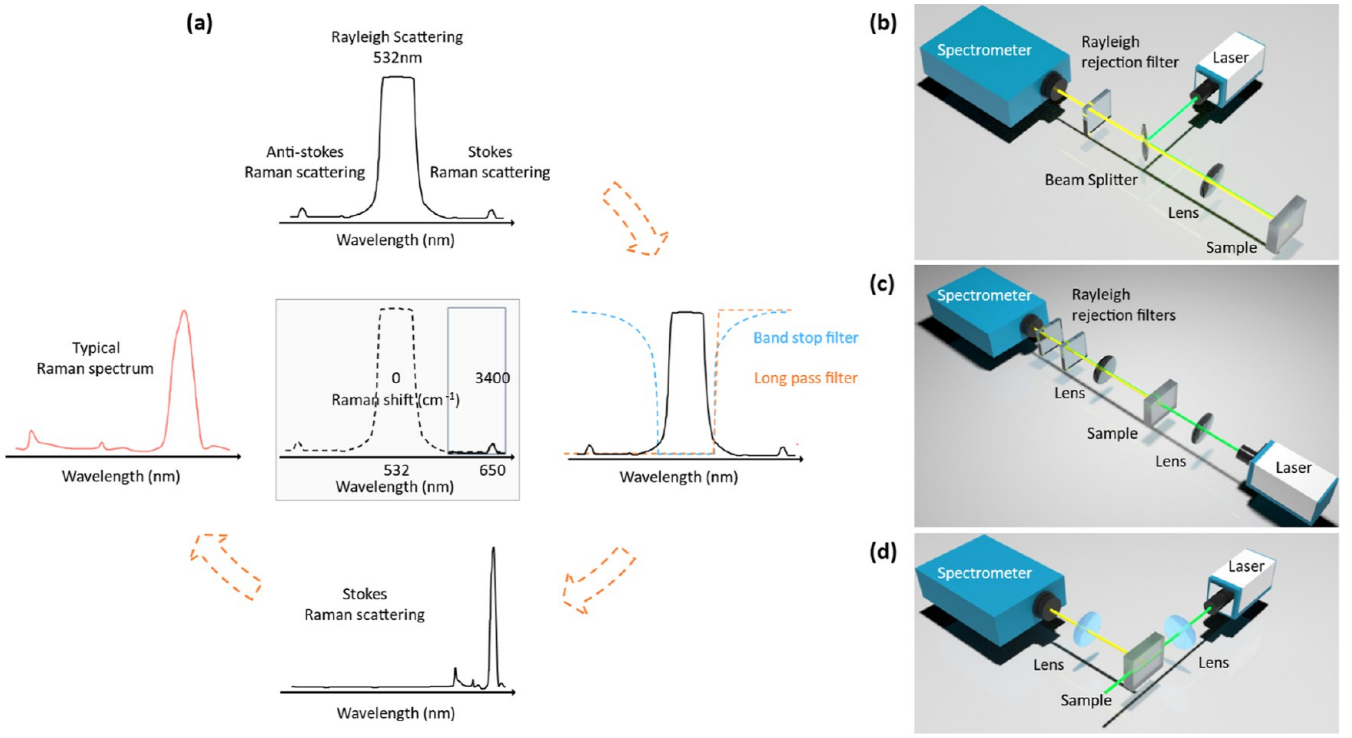

Figure 2. Characteristics of Raman spectroscopy. (a) The function of band-pass and long-pass filters in signal generation. Raman instrument optical configurations: (b) backscattering-based, (c) transmission-based, and (d) right-angle configurations. Both the backscattering-based and transmission-based configurations necessitate the use of Rayleigh suppression filters to mitigate unwanted signals caused by back reflection from the excitation source and Rayleigh scattered light. In contrast, the right-angle geometry exhibits minimal noise, obviating the need for rejection filters.

Stokes Raman scattering and anti-Stokes Raman scattering, respectively. Figure 1c illustrates the energy transitions associated with light scattering. In Raman spectroscopy, a sample is illuminated with coherent laser radiation to generate scattered light. This interaction results in a shift in radiated photon energy emitted due to the incident light frequency.[28] The alteration in vibrational energy corresponding to the scattering of light is quantified in wavenumbers, making a change in wavenumber the measure for characterizing the scattering. Figure 1d demonstrates the Raman effect. A 532 nm monochromatic incident laser having a wavenumber of 18,797 cm^{-1} undergoes scattering, resulting in a 650 nm wavelength and 15,385 cm^{-1} wavenumber. The change in wavenumber (3400 cm^{-1}) observed, also referred to as the Raman shift, provides insights into the changes occurring in molecules. This includes low-frequency, rotational, and vibrational changes. The Raman shift, denoted by the change in wavenumber (e.g., 3400 cm^{-1}), offers insights into the low-frequency, rotational, and vibrational transitions taking place within the material being examined.

The acquired spectrum resulting from the scattering of incident light exhibits three predominant scattering signals: anti-Stokes, Stokes, and Rayleigh. Rayleigh-scattered photons yield the highest intensity because they are prevalent in elastic scattering, constituting a significant portion of the emission. To obtain a reliable Raman signal during analysis, it is imperative to implement Rayleigh rejection filters, as demonstrated in Figure 2a. These rejection filters mainly consist of notch and long-pass filters. The notch filter plays a vital role in removing undesired background interference originating from Rayleigh scattering. It selectively blocks or filters out light signals from Rayleigh scattering while allowing the passage of Raman scattering light signals. Conversely, the long-pass filter is designed to eliminate undesired higher-frequency components from the scattered light while permitting lower-frequency components to pass through. Its principal purpose is to block Rayleigh scattering and higher-frequency background light, thereby facilitating the detection and analysis of Raman scattering signals, which generally exhibit lower frequencies than incident laser light.[29] The required frequency-response characteristics of the rejection filters define the specific optical layout employed for the Raman spectrometer.

Figure 2b–d visually illustrate the integration of these filters into Raman spectrometer setups. The backscattering configuration (Figure 2b) produces robust Raman spectra and is commonly used in commercial Raman spectrometers. However, this configuration is associated with significant noise caused by Rayleigh scattered light signals and laser source back-reflection. Therefore, it is essential to include beam splitters (dichroic mirrors) and Rayleigh suppression filters to ensure the generation of a high-quality Raman spectrum. In the transmission geometry (Figure 2c), the use of dichroic mirrors is unnecessary as the incident light is transmitted into the spectroscope. Nevertheless, The measurement of the spectrum in this Raman configuration is hindered by the intense incident light beam.[30] As a result, the application of noise reduction filters and high-performance laser cleaning is crucial for obtaining a high-quality Raman spectrum. In an orthogonal configuration (Figure 2d), excitation occurs at a 90° angle. This leads to minimal noise generation, rendering rejection filters unnecessary. Additionally, the optics for collecting scattered light in the right-angle geometry cover a wide area. It is more straightforward to

https://doi.org/10.1021/acsomega.4c04676
ACS Omega 2024, 9, 42822−42838

characterize a large sample, such as the overall composition of a turbid medium, in this configuration.[30]

Commercial Raman instruments are very expensive, placing them beyond the reach of the general populace. Particularly, the price of Raman microscopes often exceeds $200,000,[31] while the price of typical commercial Raman spectrometers starts at $27,000. Table 1 depicts the start pricing of Raman

Table 1. Cost of Commercial Raman Spectrometers from Reputable Optical Instrument Companies

company	model	power (mW)	wavelength (nm)	price
Thermo Fisher Scientific[33]	TruScan RM Next Generation	250	785	$86,500.00
Thorlabs[34]	RASP2	150 and 300	680 and 785	$37,740.00
Thermo Fisher Scientific[35]	TruNarc	250	785	$32,400.00
Thorlabs[34]	RASP1	300	785	$27,540.00
Thunder Optics[36]	Eddu Raman System	300	532	$10,140.00
present work	N/A	200	532	$3074.10

spectrometers with comparable wavelengths offered by respected manufacturers of optical instruments. This highlights the need for more accessible alternatives. To address this, there have been concerted efforts to devise more economical alternatives for Raman spectroscopy, with notable contributions detailed in Table 2. Johnson et al.[32] showcased the construction of a modular Raman spectrometer using commercial components, allowing for straightforward alignment and rapid collection of Raman and resonance Raman spectra from diverse solid samples. The crucial elements of the system include a spectrometer with CCD detection, a narrow-bandpass holographic filter, and a compact, cost-effective solid-state laser. The authors assert that the assembled system outlined in this paper has the potential to yield substantial cost savings, potentially amounting to several thousand dollars when compared to conventional commercial Raman systems. This is particularly true if certain components of the system are already present in the laboratory.

DeGraff et al.[37] outlined an affordable modular Raman apparatus utilizing CCD detection, achievable through the assembly of commercial components at a cost under $5000. The setup employs a spectrometer, Ocean Optics S2000/PC1000, originally designed for regular absorbance analyses. The authors present three distinctive applications: a resonance Raman experiment, a Raman polarization experiment, and a proof of the vibrational isotope effect. Mohr et al.[38] detailed the production and functionality of a cost-effective modular Raman system assembled for less than $5000. The employed monochromator and low-power green laser pointer serve as the foundation of this spectrometer. The monochromator is equipped with a linear detector array, glass fiber optical connectors, and a USB connection that functions as both a data transfer and power source. Young et al.[39] demonstrated the feasibility of using an affordable miniaturized Raman system as a substitute for a larger, more expensive conventional Raman spectrometers. The development of this system involved the methodical replacement of larger, more expensive components of existing Raman spectroscopy systems with smaller, more readily available commercial substitutes.

Montoya R et al.[40] outlined the production and performance of a homemade transmission-mode Raman system, designed for signal excitation of transparent liquid samples using a green laser pointer. The light detector employed in this low-cost and easily constructible homemade Raman spectrometer is the CMOS light sensor found in EOS DSLR cameras intended for consumer use. The system achieves a spectral resolution of about 15 cm^{-1}. The paper details the setup and discusses the performance of the spectrometer, emphasizing its affordability and simplicity. It also showed and studied Raman spectra for a variety of liquid samples and mixtures including benzene and ethanol. Aydogan et al.[41] presented an economical and user-friendly Raman spectrometer, constructed using readily available electronics, optics, and 3D printing. The optical configuration adopts a Crossed Czerny-Turner spectrometer, incorporating a linear CCD module controlled by a Nucleo F401RE and Raspberry Pi. The study focuses on obtaining Raman spectra of rhodamine B liquid, with a primary challenge being the reduction of noise arising from the laser, container, CCD, and heat. Although these earlier works demonstrated lower costs than commercial Raman spectrometers, structural and cost issues persisted resulting from challenges with light path and the integrated usage of costly spectrometers, which also hinders design flexibility.

Herein, we focus on creating an affordable and accessible Raman instrument using 3D printing technology. We aim to overcome financial barriers that often limit the use of Raman spectroscopy. The developed system was designed to be outfitted with both a spectrometer and a camera, enabling the acquisition of Raman signals and images, respectively. While only one mode can be active at any given time, this remarkable versatility provides a distinct advantage, allowing researchers to seamlessly switch between spectroscopic and microscopic analyses based on their specific research needs. By carefully selecting components and utilizing 3D printing, we've significantly reduced costs without compromising functionality and precision. The result is a reliable system capable of accurately reproducing standardized Raman spectra for various test samples. This achievement not only makes Raman spectroscopy more financially feasible but also showcases the

Table 2. Noteworthy Contributions in Economical Raman Spectroscopy Solutions

configuration	laser	power (mW)	wavelength (nm)	detector	cost	source
~45°	YAG laser	20	532	Ocean Optics HR2000	$6500.00	32
right angle	Nd:YAG laser	10	532	Ocean Optics S2000	$5000.00	37
backscattering	laser pointer	4	532	CCD Array	$5000.00	38
backscattering	laser pointer	20	532	Ocean Optics SD2000	$3700.00	39
backscattering	He−Ne laser	30	633	Ocean Optics HR4000	$3000.00	42
transmission	laser pointer	<100	532	Digital Camera	$3000.00	40
backscattering	laser pointer	200	532	Compact CCD CCS100	$3074.10	present work

https://doi.org/10.1021/acsomega.4c04676
ACS Omega 2024, 9, 42822−42838

potential of 3D printing in advancing scientific instruments. Our work introduces an innovative method for Raman detection, by offering a multimodal approach that concurrently captures Raman spectrum and image data. Beyond traditional applications, we demonstrate color-based alcohol detection, showcase a high signal-to-noise ratio (SNR) achieved through meticulous hardware meticulous hardware design and signal processing, and present a cost-effective, modular design utilizing 3D printing technology. These advancements not only enhance analytical capabilities but also inspire future developments in cost-effective Raman instruments for diverse applications.

The manuscript follows a structured progression, commencing with an introduction that provides an overview of Raman spectroscopy and its significance, as well as a cost analysis of our prepared Raman probe. The Experimental Section delves into the materials, hazards, Raman probe configuration and assembly, design of support components, discussion on lens lid and stage parts, analytes detection through Raman signal and imaging, and conclusion. A dedicated subsection on hazards ensures a comprehensive understanding of safety protocols. The detection through Raman signal and imaging section presents the outcomes of the study, including analyses of individual samples, and chemical mixtures. Finally, the conclusion encapsulates the key findings and their implications, offering a summary of the present work.

2. EXPERIMENTAL SECTION

2.1. Materials. High-purity methanol (99.5%) and ethanol (99.5%) were procured from DAEJUNG reagents chemicals and metals co, Ltd. in Korea. Deionized water, sourced from a Millipore Milli-Q system (with a resistivity of 18.2 MΩ cm at 25 °C), was utilized for all experimental procedures. The Raman probe design was conceived through computer-aided design (CAD) and brought to fruition using a 3D printer with a print precision of ±0.2 mm (model Flashforge Guider II, Zhejiang Flashforge 3D Technology Co., Ltd., Jinhua, China), employing polylactic acid (PLA) material with a filament thickness of 1.75 mm. Necessary components, including the Spectrometer (CCS100, wavelength range: 350−700 nm, resolution: 10 px/nm, detector range: 350−1100 nm, grating: 1200 lines/mm, 500 nm Blaze, CCD pixel size: 8 μm × 200 μm), Cage Assembly Rod (ER3), and Beam splitter (25 mm, EBS1 50:50), were procured from Thorlabs. A Notch filter (12.5 mm, 532 nm, OD 4.0) was sourced from Edmund Optics, while the Laser (532 nm, 200 mW) was acquired from CHRONOS. It is important to note that a laser line was not employed in the setup. The incorporation of a laser line filter could significantly contribute to signal precision but would also introduce an additional cost and potentially limit accessibility, especially in educational and resource-limited settings. In addition, CMOS camera (model MEE-700, 400−1000 nm) was procured from Srate, China. Further details regarding the costs can be found in Table 3 below. All reagents and chemicals employed in the study adhered to analytical grade standards.

2.2. Hazards. To maintain personal safety, it is highly advised to use protective gloves and glasses. When operating 3D printers, it is crucial to handle them with care and adhere to proper safety protocols due to the elevated temperatures required for melting plastic filaments. When handling chemicals, you should wear gloves and splash goggles. Glass containers with lids should be used for volatile chemical analysis. Always employ custom-made sample holders, preferably in black, to confine radiation and minimize reflections. Be sure to wear gloves when making electrical connections and take precautions to prevent short circuits and overheating. When operating the equipment, it is crucial to adhere to safety protocols, which include the use of laser goggles. Additionally, it is advisible to remove any jewelry that may produce unexpected light reflections, such as rings, bangles, and watches. During the laser alignment phases, it is imperative not to permit the entry of other staff members into the room. Maintain adequate beam barriers around the apparatus to shield individuals from stray reflections. Improper handling of the laser can be hazardous, especially given that the 100−200 mW laser falls within the class 3B category. The localized heat generated by the laser can result in immediate and permanent damage to both the flesh and the eyes. Therefore, avoid direct eye contact with the laser or any reflected laser beams.

Table 3. Commercially Available Optical Components Employed for the Construction of the Raman Instrument

component	details	manufacturer	cost
spectrometer	CCS100, 350−700 nm	Thorlabs	$2322.27
camera	MEE-700, CMOS, 400−1000 nm	Srate	$56
notch filter	OD 4.0, 12.5 mm, 532 nm	Edmund Optics	$299.00
objective lens	M-5×, 0.10 NA, *f*-25.4 mm	Newport	$137.55
optical cable	M77L01-200 μm core, 0.39 NA	Thorlabs	$90.28
laser (continuous wave)	200 MW, 532 nm, 200 mW	CHRONOS	$76.00
cage assembly rod	ER3, qty: 8	Thorlabs	$56.00
beam splitter	EBS1 50:50, 25 mm	Thorlabs	$37.00
total			$3074.10

2.3. Raman Probe Configuration. In our experimental setup, we adhered to the schematic diagram and principles outlined in Figure 3, utilizing both in-house produced and commercial components. Despite the inherent advantage of minimal noise generation in the right-angle geometry, obviating the need for rejection filters, our experimental setup adopts the backscattered geometry. This selection is due to the heightened intensity of Raman spectra achievable in this configuration relative to the right-angle geometry. Additionally, the backscattered geometry necessitates fewer Rayleigh rejection filters and does not demand high-performance laser cleaning—an imperative consideration for obtaining high-quality Raman spectra when compared to the transmission geometry. The components vital for system assembly and alignment were custom produced in-house via a 3D printer. The core component of our setup was the OX-YT5322 laser, operating at a 532 nm wavelength, offering variable output powers of 100 and 200 mW. This laser featured a beam diameter spanning from 13 to 14 mm and operated at 12 V with a current of 1 A. Its primary function was to illuminate the analytes, inducing alterations in their internal energy states.

An indispensable component seamlessly integrated into the setup was the 0.5× objective lens. It is imperative to underscore the pivotal role played by this objective lens within the Raman probe system. It influences the quality of acquired Raman data, as it effectively carries out essential functions such as precise laser focusing and proficient

https://doi.org/10.1021/acsomega.4c04676
ACS Omega 2024, 9, 42822−42838

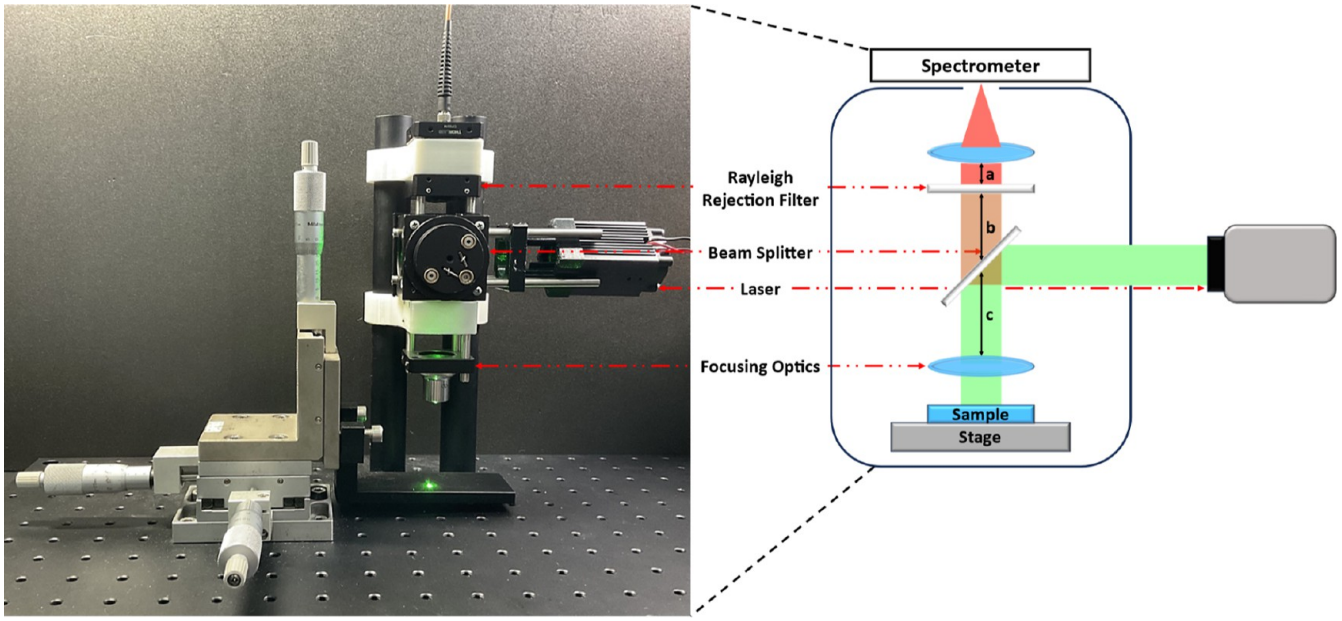

Figure 3. Integrated Raman probe. A digital image of the fully assembled setup, featuring an activated laser (left). The diagram provides a detailed schematic of the essential components, including the optical configuration, excitation source, probe optics, and detector (right). Where *a*, *b*, and *c* are 13, 40, and 63 mm, respectively.

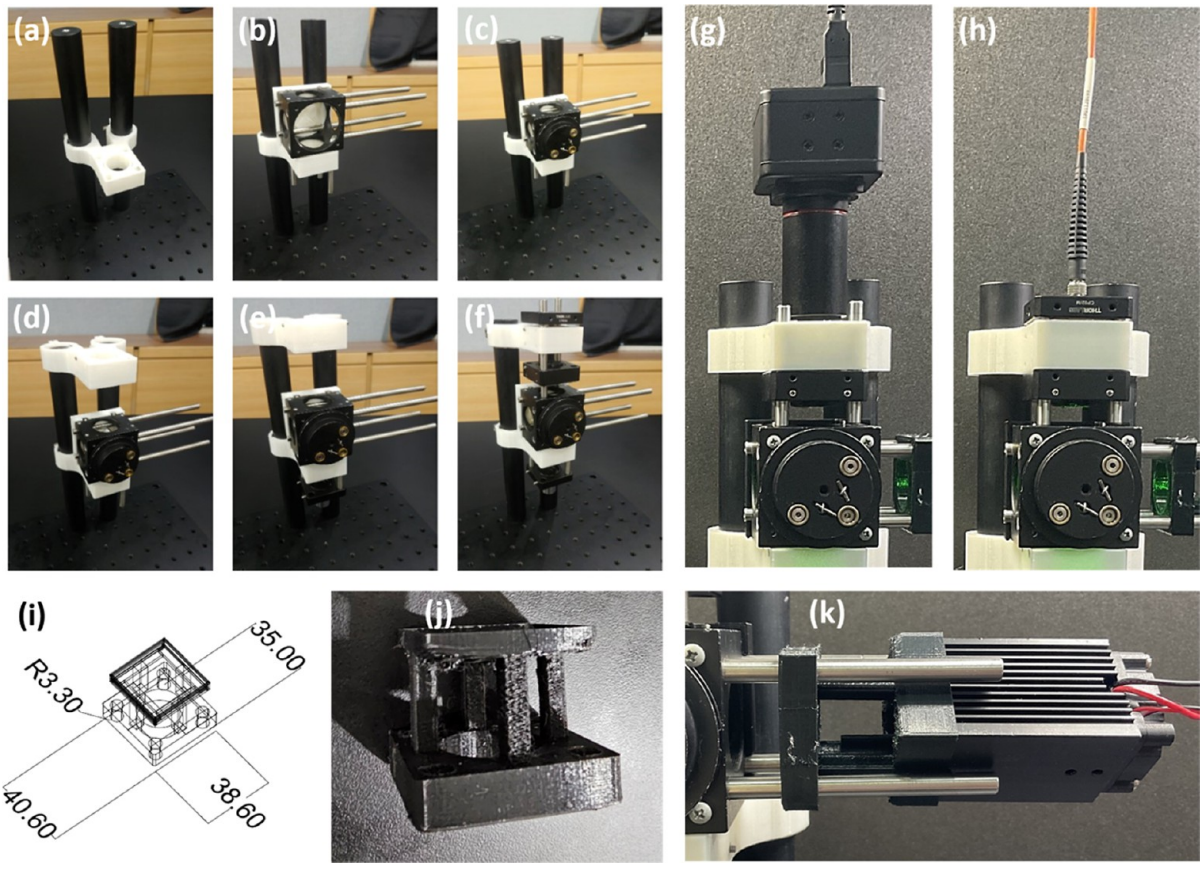

Figure 4. Assembly of the Raman probe. The assembly of components for the probe on an optical breadboard floor, including (a) single support part on pillars, (b–f) additional support parts, cage, and other components on pillars. (g) camera, and (h) spectrometer for Raman scattering measurement. (i–k) Laser alignment component. The 3D-printed laser alignment component optimizes the connection between the laser source and the assembly cage, demonstrating adaptability for various laser shapes.

collection of scattered light. To ensure optimal clarity in observing the target Raman signal, it is crucial to minimize interference arising from the more dominant form of scattering—Rayleigh scattering. In this pursuit, a carefully

https://doi.org/10.1021/acsomega.4c04676
ACS Omega 2024, 9, 42822−42838

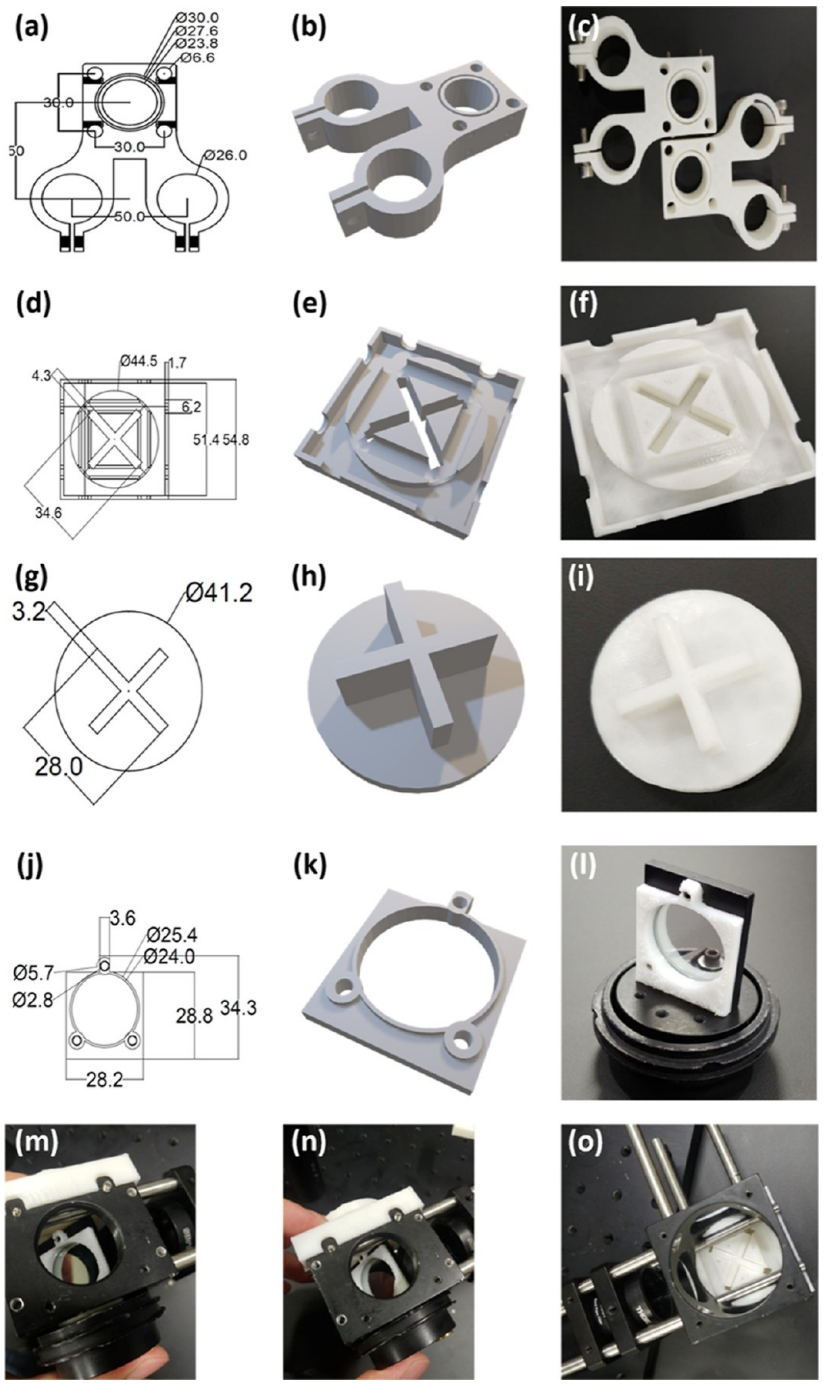

Figure 5. Support components for the Raman probe construction. (a–c) Holders for the mounted bars. (d–f) Optical cage mounting part with a 45° angled groove at the center. (g–i) Part for the safe removal of the beam splitter mounted on the cage. (j–l) Beam splitter fixing parts. (m–o) Button for easy removal.

selected 532 nm notch filter (OD4.0, 12.5 mm, sourced from Edmund Optics) was seamlessly incorporated. This notch filter adeptly attenuated the 532 nm wavelength, which aligns with the primary scattering wavelength of the laser.

For Raman spectrum acquisition, we gathered scattered light utilizing an optical cable. After securely linking the optical cable to the spectrometer, it was positioned at the focal point of our custom-built probe. After activating the laser source, the light scattered by the sample was efficiently dispersed and precisely measured, yielding a comprehensive spectrum. The spectrometer utilized in our configuration was Thorlabs' CCS100 compact spectrometer, and data acquisition was facilitated through a specialized program provided by Thorlabs. This process of spectrum acquisition entailed specific settings, with integration time variations to guarantee optimal data quality.

To further enhance the quality of our recorded spectra and mitigate any potential noise, we implemented a noise reduction technique. This approach involved acquiring the spectrum with the laser source activated and subsequently deactivated, followed by the subtraction of these two spectra. This procedure adeptly eliminated any extraneous noise, thus

https://doi.org/10.1021/acsomega.4c04676
ACS Omega 2024, 9, 42822–42838

validating the accuracy of our spectral data. To uphold the utmost precision throughout our experiments, we conducted measurements within a meticulously controlled environment, where the room was dimmed to minimize external light perturbations.

2.4. Raman Probe Assembly. Following the initial attachment of the two fixed bars to the optical breadboard floor, the assembly process commenced with the integration of supporting components to establish a robust foundation, as illustrated in Figure 4a. Following this, the cage was carefully positioned atop this supporting structure (Figure 4b). The subsequent phase involved the secure fixation of the beam splitter (Figure 4c), a critical element responsible for redirecting the laser beam to illuminate our designated target. By introducing a precise 90° deflection to the laser beam, the beam splitter facilitated the propagation of the reflected beam in a vertical direction, enabling optimal observation.

To ensure the utmost precision in horizontal and vertical alignment, we utilized elongated connecting bars, as depicted in Figure 4d. The setup also incorporated a 0.5× objective lens, bolstering its optical capabilities (Figure 4e). Another supporting element was positioned above, with a connecting bar securely fastened between the support component and the cage. To effectively eliminate Rayleigh scattering, which aligns with the wavelength of the laser, a filter was strategically inserted between the supporting component and the cage (Figure 4f).

To conclude the assembly, a laser beam input was integrated for spectral analysis, accompanied by the inclusion of a camera (Figure 4g) and an optical cable connected to the spectrometer (Figure 4h). Upon activation, the laser undergoes redirection by the central beam splitter, following a vertical trajectory, thereby augmenting the Raman effect. The utilization of an objective lens to concentrate the light onto the surface of the stage further optimizes this effect. Evidently, from the left side of Figure 3, it is apparent that the light converges to a single point on the stage, presenting a more intensified illumination. Also, a component has been incorporated at the top, featuring a strategically positioned aperture. This facilitates convenient visual observation, offering a swift and lucid view of the exact point where the laser is reflected after passing through the filter.

In addition, a laser alignment component was designed to connect the laser source to the cage assembly. As demonstrated in Figure 4i–k, this pivotal component is positioned between the horizontal bar, which extends from the cage containing the beam splitter, and the laser source. Its primary purpose is to optimize the connection between the laser source and the cage. Notably, even in the event of employing a laser with a distinct shape available in the market, the inherent versatility of the 3D printed laser alignment component allows for seamless adaptation. This ensures consistent outcomes by customizing its shape as necessitated. Such adaptability renders it an invaluable addition to the Raman probe system, assuring steadfast and dependable performance across a spectrum of laser configurations.

2.5. Support Components Design. To realize the configuration outlined in Figure 3, our initial undertaking entailed the fabrication of the primary support components, as elucidated in Figure 5. This process involved the erection of two pillars on the floor (Figure 4a), followed by the attachment of support parts to furnish a stable foundation for the placement of subsequent elements (Figure 4b). As delineated in Figure 5a–c, two apertures with a diameter of 25 mm were precisely fashioned to accommodate the supporting bar, with the center-to-center distance between these 25 mm apertures meticulously set at 50 mm to ensure the exact centering of the component. The four small circles surrounding the 50 mm apertures were purposefully incorporated to firmly anchor the vertically connected rods, facilitating the straightforward attachment and operation of various components. Given the sensitivity of the probe to movement, this part serves a pivotal support function, with its position susceptible to change under a substantial load. To counteract this, screw sockets were added around each 25 mm aperture, ensuring secure fastening to the pillars. As Figure 4f aptly demonstrates, once this support component is affixed to the pillars, its stability remains uncompromised even when subjected to the placement of numerous additional objects.

Figure 5d–f delineate the component engineered for the secure mounting of an optical cage. Within this component, laser-connecting support rods were affixed both horizontally and vertically. As a result, a designated path with a diameter of 6.2 mm, perfectly aligned with the diameter of the connecting rod, was meticulously crafted. This path accommodates multiple cage-connecting rods, permitting their unimpeded passage through both horizontal and vertical orientations. Additionally, to facilitate the entry of the laser and its redirection at a precise 90° angle toward the target sample, the cage necessitates the incorporation of a beam splitter. To address this, we integrated a 45° angled groove at the center of the component, ensuring that the beam splitter can only be seated when correctly aligned at 45 deg. This design feature mandates that, regardless of the initial orientation of the beam splitter within the cage, it must undergo exacting 45° alignment for proper mounting, thereby enabling the precise deflection of the incoming laser at a 90° angle.

In the process of mounting the beam splitter to the cage, a stage and holder were employed. However, due to the fastening of the holder with screws, there existed a notable risk of potential damage to the beam splitter if the installation was not executed meticulously. To mitigate this risk, as illustrated in Figure 5g–i, we designed a protective component intended to encapsulate the beam splitter once it was affixed to the holder. We incorporated three screw grooves into this protective component and affixed it directly to the holder using screws. This approach offers a considerably safer means of securing the beam splitter, in contrast to the application of force. As demonstrated in Figure 5m–o, the protective component assumes its designated position on the side stage. It aligns precisely with the beam splitter socket, and it is securely fastened with a screw to ensure the beam splitter is firmly and securely in place.

Since the beam splitter serves a dual function as a lens, it necessitates careful handling. Once affixed to the cage, removal can pose a significant challenge, given its firm anchoring by the cage mounting elements detailed previously. To alleviate this concern, as depicted in Figure 5j–l, we integrated a meticulously designed groove. Additionally, the designed groove ensures that the surface of the beam splitter is precisely oriented along its axis. This alignment is crucial for the proper functioning of the optical system, as any deviation could lead to undesirable optical aberrations or inaccuracies in the beam splitting process. Furthermore, we introduced a button mechanism at the rear, streamlining the removal process with a straightforward button press (Figure 5m–o). This enhance-

https://doi.org/10.1021/acsomega.4c04676
ACS Omega 2024, 9, 42822–42838

ment in design guarantees the swift and secure extraction and storage of the beam splitter, allowing for adjustments when required.

2.6. Lens Lid and Stage Parts. It is well understood that the seemingly straightforward task of positioning the lens on the probe carries the potential risk of unintended displacement and subsequent damage during adjustments. Such occurrences can lead to the deterioration or loss of functionality of the lens. To counteract these potential risks, we have conceived and implemented a protective apparatus designed specifically for the lens. This protective component not only shields the upper surface of the lens but also ensures its steadfast retention, thereby mitigating the possibility of direct contact and potential damage due to handling. Furthermore, considering the compact 12 mm diameter of the lens, we engineered a specialized component tailored for lens housing, which concurrently serves as a socket for attachment to the vertical bar, as depicted in Figure 6a−c. This socket component was

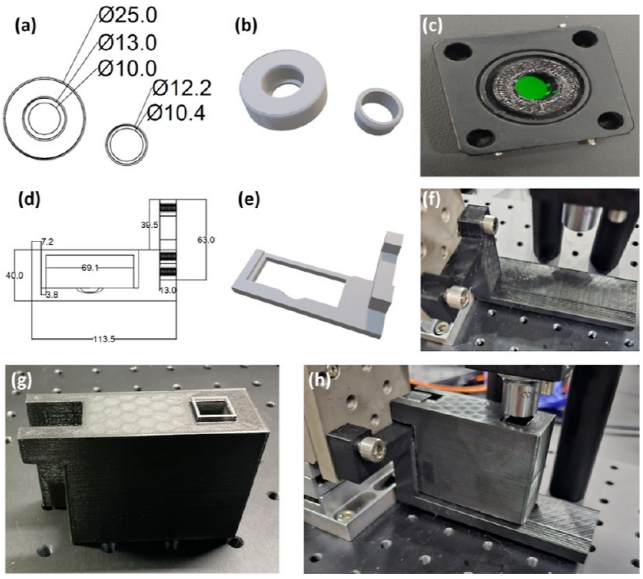

Figure 6. Lens lid and stage parts for sample observation. (a−c) Focus lens lid. (d−h) The sample stage and a socket component designed for liquid samples.

designed with a hole diameter of 25 mm, offering a snug and precise fit to ensure the lens remains securely in place during probe adjustments. This design refinement enhances the overall stability and functionality of the system.

Our primary focus in this research was on liquid samples, necessitating the provision of a suitable container or stage. We chose a cuvette, a standard choice in commercially available optical probes. Additionally, we fabricated a holder expressly designed for the glass cuvette, as extensively elucidated in Figure 6d−h. It is noteworthy that, apart from glass cuvettes, smaller containers like capillary tubes can also be employed. Figure 6d−f offer a comprehensive insight into the intricacies of the sample stage design, while Figure 6g,h provide a detailed view of the dedicated holder component tailored for liquid samples. This holder component stands as a vital addition to our system, ensuring the steadfast positioning and stabilization of samples during testing and data collection.

Furthermore, to ensure precise sample alignment, we integrated a commercially available Thorlabs ATS4XYZ 3-axis linear stage into our setup, as vividly illustrated in Figure 3. This stage distinguishes itself with outstanding precision and reliability, enabling the seamless and accurate movement of samples. Leveraging the capabilities of this advanced stage, we can meticulously position the sample holder in the desired location. Moreover, its vertical movement feature allows us to make focal adjustments, facilitating the measurement of samples of varying sizes and ensuring the acquisition of comprehensive data for our research. The incorporation of this stage markedly elevates the overall precision and efficiency of our experimental arrangement. Given the optical nature of the system, comprehensive measurements of the printed parts' dimensions were conducted using a high-precision a digital caliper (CAS Digital Vernier Caliper, DC150-1, Republic of Korea) and verified against the modeled design specifications to ensure the precision of the parts. Additionally, it is worth noting that the 3D printer utilized for fabrication has a print precision of ±0.2 mm. The conducted measurements indicate that the average size error across all components is within ±0.1 mm, which is sufficiently small relative to any optical discrepancies that may arise in reproducing the system. The 3D printed components for the Raman setup took approximately 6 h to produce, with the duration primarily influenced by the complexity and size of each part. The 3D printer used for this task operated at speeds ranging from 10 to 200 mm/s, with layer height settings typically varying between 0.1 and 0.3 mm.

3. PERFORMANCE ASSESSMENT OF THE RAMAN PROBE

3.1. Peak Intensity and SNR. Figure 7 presents a detailed analysis of the performance metrics of the Raman probe developed in this study. The investigation focused on the behavior of acquired Raman spectra. Specifically, two critical parameters, peak intensity, and SNR, were examined with respect to varying integration times. The individual Raman spectra in Figure 7a−f illustrate the characterization of the analyte at integration times ranging from 1 to 50 s. Furthermore, using the prominent Raman peak of ethanol at a Raman shift of 2930 cm^{-1} as displayed in Figure 7g, the observed variations in peak intensity and SNR are depicted in Figure 7h,i. Notably, three independent spectra were obtained for each measurement to ensure reproducibility. The error bars, which represent the standard deviation across these replicates, have been included to provide a clearer understanding of the data's variability. This investigation serves to underscore the capability of the Raman setup to achieve high SNR and highlights the potential for further enhancement through increased integration time.

In assessing the performance of our developed Raman probe, we conducted characterizations on various analytes and explored the impact of integration time on the Raman signal. Integration time, representing the duration of exposure of scattered light to the detector, plays a pivotal role in signal measurement. Longer integration times enable the collection of more photons, yielding a stronger spectrum with an enhanced SNR. To evaluate the Raman probe, we measured the Raman spectrum of ethanol at varying integration times of 1, 10, 20, 30, 40, and 50 s, as shown in Figure 7a−f. Upon increasing the integration time, we observed a linear increase in the intensity of peaks, with an R^2 value of 0.9967. The coefficient of determination R^2 was calculated using the standard formula

https://doi.org/10.1021/acsomega.4c04676
ACS Omega 2024, 9, 42822−42838

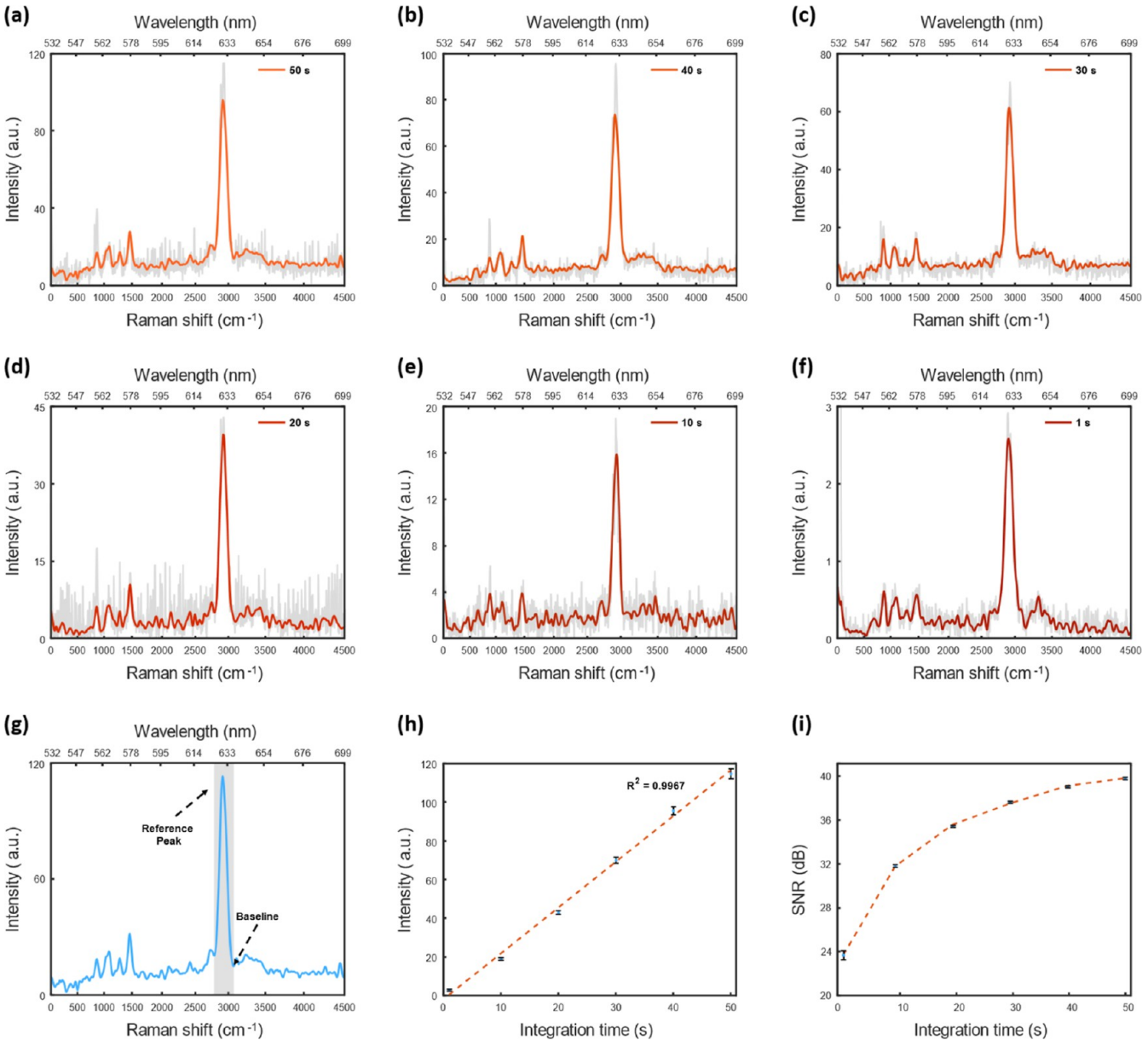

Figure 7. Raman signal analysis. Raman spectra at varying integration times of (a) 50, (b) 40, (c) 30, (d) 20, (e) 10, and (f) 1 s. The gray spectra represent the raw, unprocessed data obtained directly from the Raman measurements, while the orange spectra display the processed signal after applying background subtraction and data smoothing techniques to enhance signal clarity and reduce noise. (g) The reference peak at 2930 cm^{-1} for further analysis and an indication of the baseline for used for determining the peak height. The variations in (h) peak intensity and (i) SNR with integration time. Error bars in (h,i) represent the standard deviation across three independent measurements.

$$R^2 = 1 - \frac{\sum (y_i - f(x_i))^2}{\sum (y_i - \bar{y})^2} \quad (2)$$

where y_i represents the observed data points, $f(x_i)$ is the predicted value from the model, and $\bar{y}$ is the mean of the observed data. The peak intensity exhibits a steady increase from 2.908 to 114.897 au across the examined integration time range. This discernible trend is depicted in Figure 7h, where the peak intensity of the chosen reference peak at 2930 cm^{-1}, shown in Figure 7g, is plotted against integration time, ranging from 1 to 50 s. The observed linearity in signal intensity with increasing integration time presents a significant advantage for our developed Raman probe. Such linearity is crucial for several reasons. First, it implies a predictable and controllable behavior in signal enhancement, allowing researchers to anticipate the outcome when adjusting integration times. Second, the linear correlation signifies a reliable and systematic response of our system to varying exposure durations, providing a foundation for reproducible and consistent results. This predictability and reliability in signal enhancement contribute to the overall robustness of our Raman probe, making it a valuable tool for obtaining precise and reproducible Raman spectra across different experimental conditions and integration time settings.

Simultaneously, the plot of SNR against integration time depicted in Figure 7i reveals a similar positive correlation. The SNR, calculated based on the reference peak, increased from 23.668 to 39.657 dB as the integration time extended from 1 to 50 s. The observed enhancement in SNR further substantiates the proficiency of the developed Raman setup in discriminating

https://doi.org/10.1021/acsomega.4c04676
ACS Omega 2024, 9, 42822−42838

the analyte signal from the background noise. To quantify the SNR and further express the computed values in decibels (dB), we employed the formulas

$$\mathrm{SNR} = S/\sigma_y \tag{3}$$

$$\mathrm{SNR_{dB}} = 10\log_{10}(\mathrm{SNR}) \tag{4}$$

where S represents the average peak height within the spectral band, and σ_y is the standard deviation of the peak height,[43] which is the difference between the baseline and the peak intensities. Importantly, the baseline is chosen at a spectral shift where no peak is present, ensuring that only noise contributes to the signal within that spectral band (see Figure 7g). It is noteworthy that the SNR is determined using the measured Raman signal directly, postbackground removal, and the presented data is an average of 50 spectra measured successively.

The utilization of integration times ranging from 1 to 50 s reflects a practical and applicable time frame for capturing Raman spectra even at very short durations. The demonstrated potential for further improvement in signal quality by extending the integration time as demonstrated in Figure 7, reaffirms that the developed system exhibits consistent and reliable performance with high SNR. These findings highlight the robust performance and emphasize the versatility and adaptability of the developed Raman probe to various applications.

3.2. Noise Reduction via Optical Hardware Configuration. The achievement of a high SNR in our 3D printing-enabled Raman setup coupled with a spectrometer is underpinned by meticulous attention to optical hardware configuration. The realized SNR can be attributed to the careful consideration and alignment of various optical components, each playing a crucial role in enhancing signal quality. Optical alignment is a critical factor in our setup, influencing the overall system performance. Accurate alignment minimizes signal losses and aberrations, maximizing the collection efficiency and subsequently improving the SNR.

One pivotal aspect of our optical design involves the beam spot and precise focusing. By ensuring a well-defined and focused beam spot on the sample, we mitigate the likelihood of signal dispersion and loss, contributing to an enhanced SNR. The focused beam spot due to the focal length of the lens in the developed setup facilitates efficient interaction with the sample, promoting a stronger Raman signal. The focal length is a critical parameter in our Raman setup, as it dictates the distance over which the lens converges parallel rays of light to a focus. This careful selection of the focal length is instrumental in achieving a focused light on the sample for strong interaction. Hence, an appropriate focal length of 25.4 mm was chosen based on the optical hardware design to optimize the intensity and quality of the signal. Figure 3 depicts the various separation distances. By selecting an optimal focal length, we ensured that the Raman signals are efficiently captured, maximizing the signal strength, and contributing to a high SNR.

In addition, the use of an XYZ stage with the designed holder provides a versatile mechanism for adjusting the position of the sample within the focal plane. This adjustability is paramount in fine-tuning the spatial alignment and ensuring that the sample is optimally positioned for the Raman measurements. It allows for precise control over the focal point, thereby contributing to the optimization of the beam spot and intensity on the sample. Thus, placing the analyte in the focal plane enhances the efficiency of the Raman signal generation process, as it corresponds to the region where the light is most concentrated. In our setup, meticulous attention is paid to aligning the focal plane precisely with the region of interest in the sample. This precision ensures that the Raman signals are selectively collected from the desired location, allowing for detailed and accurate chemical analysis. The controlled alignment of the focal plane not only improves spatial resolution but also minimizes unwanted contributions from adjacent areas, thereby reducing background noise and enhancing the overall SNR. Beyond the primary objective of achieving optimal beam characteristics, the careful consideration of the focal length, coupled with the purposeful design of the sample holder with the stage, serves the additional crucial roles of minimizing signal dispersion and maximizing the SNR in the Raman signal. The collective synergy of these factors enhances the performance and sensitivity of developed Raman spectroscopy system resulting in a high SNR.

3.3. Noise Reduction via Signal Processing. In our pursuit of a high SNR and the accurate discernment of characteristic peaks in the Raman spectrum, additional precautions were implemented. Two key strategies, namely background subtraction and local regression data smoothing with high sensitivity to local variations using MATLAB (Version R2022b, MathWorks, Natick, MA, USA), played pivotal roles in enhancing the overall quality and reliability of our experimental results.

Background subtraction is a critical step undertaken to mitigate the influence of extraneous signals or noise that may obscure the true Raman signature of the sample. The background spectrum exhibits characteristics unrelated to the sample, possibly arising from factors such as instrumental noise, baseline drift, or contributions from the surrounding environment. The subtraction of the background spectrum serves to isolate the specific signal obtained from the sample, thereby improving the clarity and precision of the collected data. By carefully subtracting the background signals from the raw Raman spectrum, we effectively isolated the genuine Raman scattering contributions originating from the sample. This approach aids in uncovering subtle spectral features and ensures that the obtained Raman spectrum is an accurate representation of the intrinsic characteristics of the sample. The implementation of background subtraction is a standard practice in Raman spectroscopy, and our adherence to this technique underscores the precision and rigor embedded in our methodology.

To further enhance the clarity and interpretability of the Raman spectrum, a local regression data smoothing with high sensitivity to local variations technique was employed. This method involved fitting a regression curve to the data points within a localized region, effectively reducing noise and fluctuations without compromising the integrity of the underlying signal. A key feature of this approach was the utilization of an extremely small smoothing span, less than 0.020. This value choice reflects our commitment to addressing local variations with high sensitivity. The use of a minimal smoothing span ensured that the local regression process responded keenly to subtle changes within the spectrum, capturing intricate details while maintaining the overall signal integrity. By adopting a local regression approach, we achieved a balance between noise reduction and preservation of the characteristic peaks. This refinement is

https://doi.org/10.1021/acsomega.4c04676
ACS Omega 2024, 9, 42822−42838

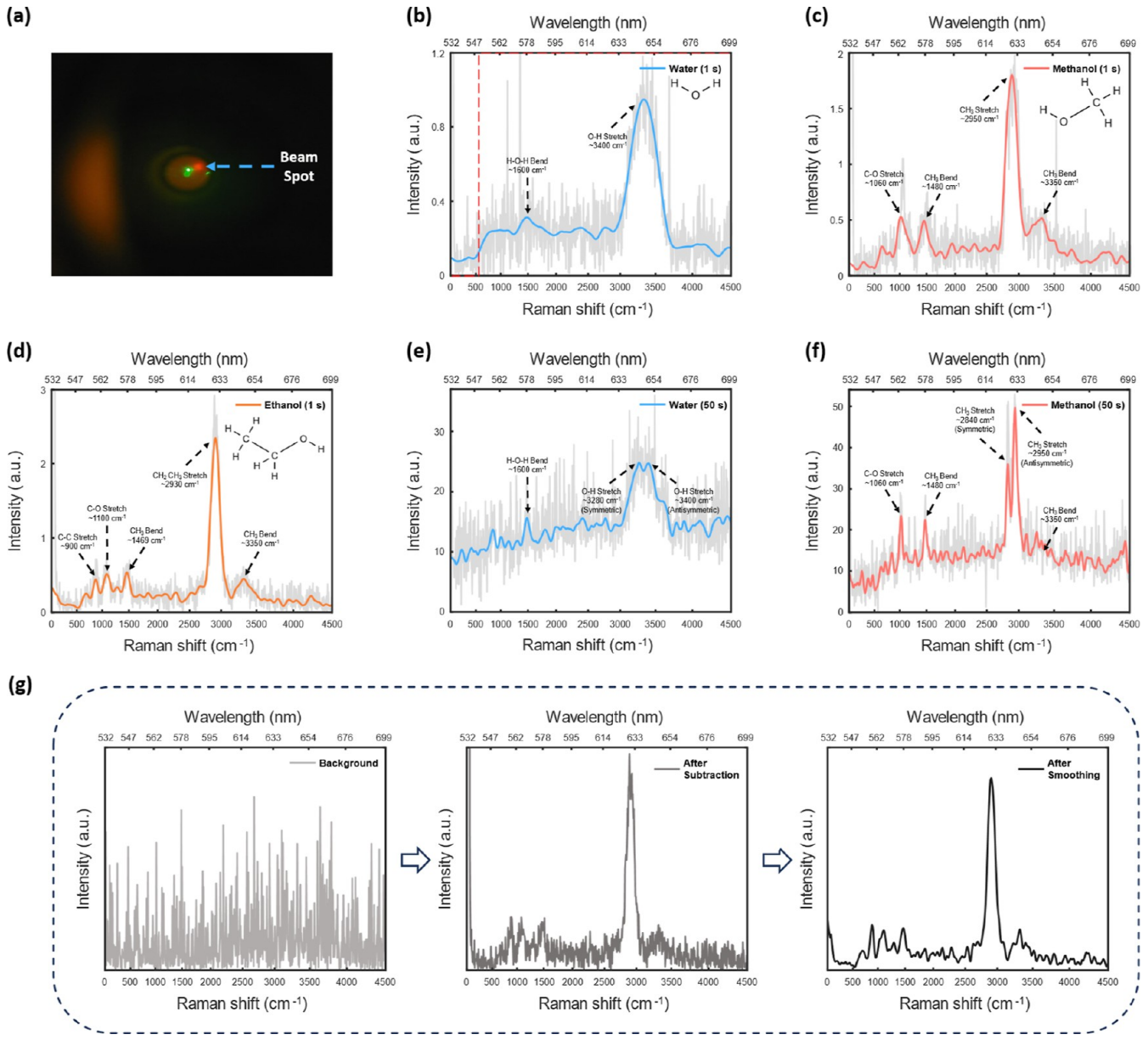

Figure 8. Characterization of various liquid analytes. (a) Observed laser beam spot. (b) Measured Raman spectra of water with bandpass filter curve overlaid (red dash lines), (c) ethanol and (d) methanol, at an integration of 1 s. Raman spectra of (e) water and (f) methanol acquires at an integration of 50 s. The gray spectra represent the raw data, while the blue, red and orange spectra display the processed signal after background subtraction and smoothing. The measured Raman spectra have a spectral resolution of 7.5 cm^{-1}. (g) Stages involved in the signal processing of the acquired Raman spectra.

particularly valuable when dealing with subtle features in the spectrum, as it facilitates a more accurate identification and quantification of peaks, ultimately contributing to the achievement of a high SNR.

The combination of background subtraction and local regression data smoothing with high sensitivity to local variations reflects a comprehensive strategy to optimize the quality of our Raman spectra. These precautions not only address issues related to noise but also enhance the discernibility of characteristic peaks, especially in the presence of complex sample matrices or low-concentration analytes. The resulting high SNR ensures a robust foundation for the interpretation and analysis of the Raman data, bolstering the reliability and significance of our experimental findings.

3.4. Detection via Raman Signal and Imaging. In our experimental setup featuring the constructed Raman probe, we conducted a series of measurements to obtain the Raman spectra of key test samples, namely water, methanol, and ethanol. Figure 8a highlights the beam spot observed during the analysis. Given that the 650 nm wavelength corresponds to red, a direct inference can be drawn. Thus, the prominent red spot, positioned adjacent to the green spot on the left side, signifies the Raman signature of water. This distinctive visualization provides a clear indication of the unique vibrational properties of water under Raman microscopy.

As illustrated in Figure 8b–f, the x-axes represent the wavelength (λ) at the top, and the inverse of wavelength ($1/\lambda$) at the bottom, indicating the wavenumbers for the Raman shift. Significantly, the outstanding peak of Figure 8b, observed at a

https://doi.org/10.1021/acsomega.4c04676
ACS Omega 2024, 9, 42822−42838

wavenumber of 3400 cm^{-1}, corresponds to an approximate wavelength of 650 nm. This prominent feature indicates a substantial energy transition within the sample under examination. Figure 8c,d distinctly exhibit the Raman spectra corresponding to methanol and ethanol, respectively. These spectra exhibit the characteristic multiple peaks that are well-established for these liquid samples, aligning consistently with reported findings.[44−46] The developed Raman probe successfully derived characteristic vibrational modes, specifically the stretching and bending modes, corresponding to each of the analytes—water, methanol, and ethanol—as shown in the acquired Raman spectra. This analytical performance is noteworthy as it provides valuable insights into the molecular composition and structure of the liquid samples under investigation. Notably, the developed system exhibited the ability to distinguish characteristic peaks of the various analytes, even at a brief integration time of 1 s, as depicted in Figure 8b−d. This remarkable capability not only underscores the high performance of the developed system but also emphasizes its consistency, rendering it well-suited for dynamic processes. In scenarios where the sample being characterized undergoes rapid changes over short time scales, this capability of our system enables more effective capture of these changes.

In addition, Figure 8e,f shows the measured Raman spectra of the analytes at an integration time of 50 s (see Figure 7a for ethanol). The quality of the measured signals significantly improved at this extended integration time, providing higher signal intensities, and revealing intricate details of the analyte, such as the symmetric and antisymmetric stretching of O−H and CH_3 for water and ethanol, respectively. This demonstrates the potential of the developed system to detect analytes with high sensitivity. This exemplary outcome attests to the capacity of the system to provide higher signal quality during prolonged integration times. This also demonstrates its versatility and adaptability across a wide range of experimental requirements, enhancing its utility in diverse research applications. Furthermore, this congruence affirms that the developed Raman probe correctly reproduces the established Raman spectrum for each sample, effectively mirroring the performance of expensive commercial-grade Raman instruments. Figure 8g outlines the three critical stages in the processing of Raman spectra. The first stage (left), acquired background spectrum, shows the raw spectrum of the baseline noise and potential interferences. The second stage (middle), Raman spectrum after background subtraction, depicts the spectrum following background subtraction, where baseline signals and unwanted noise have been removed to reveal the true Raman signals. The final stage (right), Raman spectrum after smoothing, presents the processed spectrum with applied smoothing to reduce noise and enhance clarity. This sequence effectively demonstrates the data processing steps, leading to a more accurate and interpretable final Raman spectrum.

To further bolster the credibility of our Raman spectrum recordings, we proceeded to conduct experiments involving mixtures of water and ethanol at diverse concentrations. This additional experimentation will serve to validate the accuracy and reliability of our recorded spectra. The objective of these experiments was to evaluate the capacity of the self-constructed Raman probe to accurately discern and characterize mixed samples. To achieve this, we prepared solutions of two distinct samples—water and ethanol—and subsequently conducted measurements to assess the performance of the developed probe. The obtained spectra were a result of systematically altering the volume proportions of ethanol, distinguished by its notable intensity, and water, characterized by its discernible spectral shapes. This systematic adjustment encompassed the following water-to-ethanol ratios, detailed in Table 4.

Table 4. Water to Ethanol Ratios, and Corresponding RGB Values

water−ethanol ratio	R/G/B values (calculated at the center)
9:1	220:87:20
7:3	186:42:7
5:5	234:114:27
3:7	248:132:29
1:9	250:151:32

Figure 9a provides a visual comparison with blank cuvettes prior to light exposure. As shown in Figure 9b, the cuvettes containing ethanol−water mixture were arranged in a progressive sequence of increasing ethanol concentration from left to right. The accompanying cuvette image serves to vividly illustrate the noticeable shift in coloration as ethanol concentration rises. Complementing this visual data, Figure 9c presents optical images at an exposure time of 33 ms, further substantiating the observed transition from red to yellow hues. For a comprehensive quantification of these color changes, Table 4 provides the corresponding RGB values, which exhibit substantial alterations as ethanol concentration increases. The RGB values were determined by selecting a defined region of interest (ROI) within the acquired images to exclude the green laser beam spots, ensuring that the analysis focused solely on the color changes in the ethanol−water mixtures. MATLAB (Version R2022b, MathWorks, Natick, MA, USA) was then employed to extract the corresponding RGB values from the ROI, using MATLAB's built-in functions "imrect" and "imread", providing quantitative data for further analysis.

The correlation between color shifts and alcohol concentration, as observed in our study, introduces an additional dimension to the analytical framework. While the initial focus was on quantifying concentration through Raman spectrum analysis, the integration of a camera and a tube lens into the system revealed a concentration dependent color shift. This finding expands the potential avenues for substance detection and analysis, providing a more comprehensive understanding of the interplay between optical configurations and substance characteristics. The collective observations suggest that the dual modality of our custom setup lays the groundwork for the development of an affordable alternative to commercially available Raman microscopes, offering comparable performance levels. This underscores its efficacy and reliability in delivering accurate Raman characterization. This achievement marks a significant milestone in the development of cost-effective Raman spectroscopy tools.

Three independent spectra were acquired for each ethanol−water mixture concentration. The area under the curve for the most prominent peak (2750−3100 cm^{-1}) was calculated for each measurement. The standard deviations of these values have been represented as error bars in the revised Figure 10, ensuring a clear depiction of the data's variability and reinforcing the statistical validity of the results. Upon examining the Raman spectra presented in Figure 10a, a discernible trend emerges as the ethanol concentration increases from 10% to 90%, the characteristic ethanol peak exhibits a consistent linear increase. This observed pattern is

https://doi.org/10.1021/acsomega.4c04676
ACS Omega 2024, 9, 42822−42838

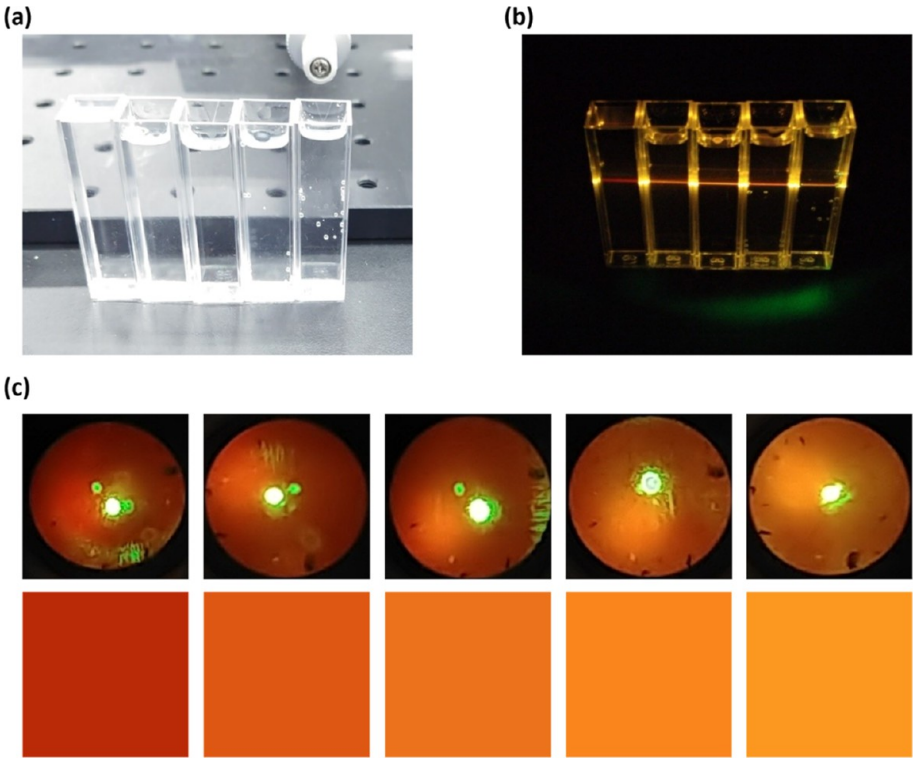

Figure 9. Visualization of ethanol−water solution. (a) Sample cuvettes with analytes for comparison. (b) Cuvettes containing ethanol−water solutions with a gradual increase in ethanol concentration from left to right. The image shows the color changes corresponding to the increasing ethanol concentration. (c) Corresponding Raman spectra for each cuvette, accompanied by their RGB color images profiles, illustrating the direct correlation between the Raman spectral data and visible observed color shift as ethanol concentration increases. This correlation emphasizes the system's capability to link spectral changes with visible color changes, offering a dual-mode approach for analyzing substance concentrations.

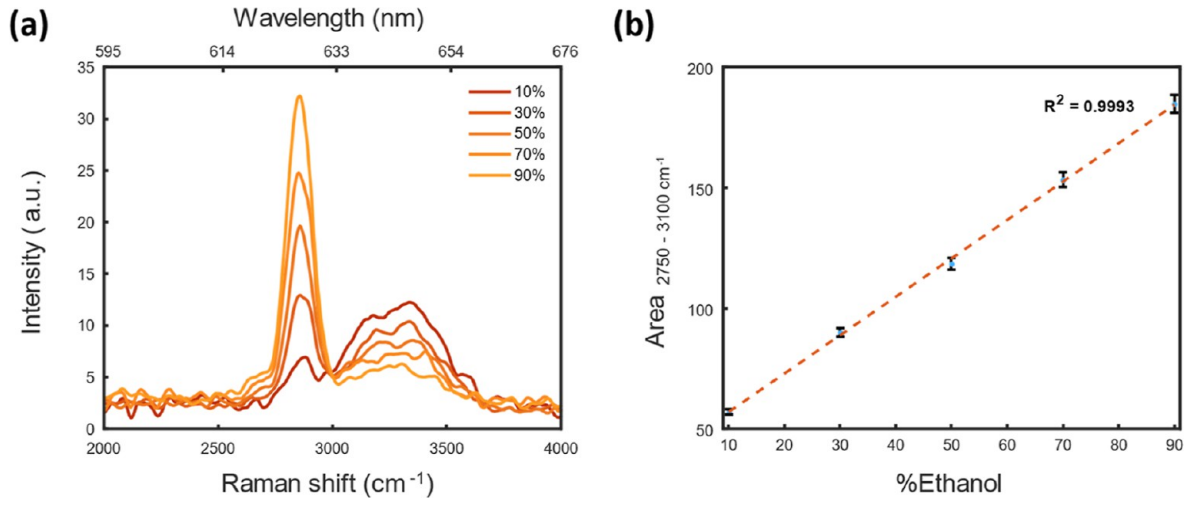

Figure 10. Raman spectra of ethanol−water solution. (a) Plot of the acquired Raman spectra for the solution of water and ethanol at different concentrations of ethanol. (b) The corresponding area plot of the most prominent peak for three batches, located at 2750−3100 cm^{-1}, exhibits an R^2 value of 0.9993, indicating a strong linear relationship.

further illustrated in Figure 10b, which depicts the corresponding area plot of the characteristic peak spanning from 2750 to 3100 cm^{-1}, demonstrating a strikingly linear progression, supported by an R^2 value of 0.9993. These results instill a high level of confidence in the fidelity of the observed variations when assessing the samples through the Raman probe we constructed, affirming that they accurately reflect the Raman spectra of the samples. This outcome validates the accuracy and reliability of our experimental setup.

4. CHALLENGES AND STRATEGIES FOR DEVELOPING THE RAMAN PROBE

In examining the robustness of our experimental methodology, we must acknowledge the potential challenges in reproducing the results in different setups. Our study has provided comprehensive documentation on the experimental setup, including key parameters, methodologies, and detailed material specifications. The modular design and incorporation of 3D printing technology for diverse components significantly boost

https://doi.org/10.1021/acsomega.4c04676
ACS Omega 2024, 9, 42822−42838

the potential for reproducibility. This approach, while contributing to cost-effectiveness, introduces challenges stemming from the inherent variability in 3D printing materials and techniques. The potential for failure could result from variations in the quality and precision of 3D-printed components, which may impede the straightforward replication of the experimental setup. Additionally, the accessibility and availability of comparable 3D printing technology and selected components can differ across locations and institutions, introducing potential variability that may influence the ease of reproducing our results.

Another limitation of our approach resides in the utilization of a low-cost spectrometer, resulting in relatively lower spectra resolution. Consequently, our system may encounter challenges in accurately detecting certain peaks. This limitation underscores the trade-off between cost-effectiveness and the potential compromise in spectral resolution. Our system is well-suited for straightforward detection purposes, making it particularly suitable for educational settings or learning purposes. However, for more advanced applications, an upgrade involving advanced components such as high-resolution spectrometers, lenses, and lasers becomes imperative. Notably, samples characterized by exceptionally weak Raman signals or those susceptible to fluorescence interference may pose challenges, hindering the attainment of precise measurements. It is crucial to recognize that our procedure is specifically optimized for a spectrum of common sample types. Consequently, we advocate for meticulous consideration of sample properties when implementing the method to ensure optimal outcomes.

Furthermore, our focus on a specific set of liquid samples—water, methanol, and ethanol—gives rise to concerns regarding the generalizability of our findings to a broader spectrum of samples with diverse chemical compositions. Assumptions about linearity in the Raman spectra, especially concerning alcohol concentration, present a potential limitation, as this linearity may not hold for all types of mixtures or analytes. This emphasis on relatively simple liquid samples also leaves the applicability to more complex mixtures and solid samples as an unresolved question. Additionally, the inclusion of the Thorlabs ATS4XYZ 3-axis linear stage, while contributing precision, is not without limitations in terms of availability and cost. However, given the study's specific focus on simple samples, it is crucial to highlight that the absence of the linear stage would not significantly compromise the system's performance in the conducted experiments.

The design of our system exhibits considerable flexibility, enabling the use of various additive manufacturing techniques beyond fused filament fabrication. For applications demanding higher precision or distinct material properties, techniques such as stereolithography (SLA) and selective laser sintering (SLS) offer viable alternatives.[47,48] SLA, which employs photopolymer resin cured by a laser, provides superior surface finishes and intricate detail, while SLS, which utilizes powdered materials such as nylon, affords enhanced mechanical strength and thermal resistance. Moreover, material selection can be customized to meet specific experimental needs. While PLA was used in this study due to its ease of use, alternative materials such as acrylonitrile butadiene styrene, polyethylene terephthalate glycol, or high-performance polymers such as polyether ether ketone can be considered to address requirements for greater durability, flexibility, chemical resistance, or thermal stability. This adaptability in both manufacturing techniques and materials ensures that the components of our Raman setup can be precisely tailored to suit a diverse array of experimental conditions and applications.

To elevate the accuracy and robustness of our experimental setup, several improvements can be considered. Exploring advanced signal processing algorithms based on machine learning (ML) and deep learning (DL) for highly sensitive detection represents a promising avenue. Additionally, advanced noise reduction techniques should be explored to enhance SNRs, especially in challenging environments. The integration of state-of-the-art optics to achieve enhanced sensitivity and resolution is another suggested enhancement. Diversifying the sample set to include a broader variety of samples would provide a more comprehensive understanding of the system's capabilities and limitations across different chemical compositions. Incorporating calibration and validation standards is essential for ensuring the accuracy and reproducibility of the Raman probe. Providing explicit details about 3D printing material properties is crucial for consistency and reliability in the construction of components. Implementing rigorous environmental controls is important for minimizing external influences on the Raman spectrum. Furthermore, investigating nonlinear calibration models, especially if the relationship between Raman signal and analyte concentration is not strictly linear, ensures accurate predictions across a wider range of concentrations.

5. CONCLUSIONS AND FUTURE WORKS

In conclusion, this study demonstrates a cost-effective and user-friendly method to create a versatile Raman instrument capable of handling both spectroscopic and microscopic analyses. Utilizing a multimodal approach that captures Raman spectrum and image data, we demonstrate an innovative application through color-based alcohol detection. Our methodology achieves a high SNR through meticulous hardware design and signal processing, and we emphasize a cost-effective and modular design that leverages 3D printing technology. By employing carefully selected components and employing 3D printing technology, we assembled a functional Raman probe system. The constructed instrument demonstrated exceptional performance in replicating standardized Raman spectra for various test samples, namely water, ethanol, and methanol. Furthermore, experiments involving mixtures of water and ethanol at different concentrations underscored the efficiency of the probe in discerning mixed substances accurately.

The systematic analysis of Raman spectra about ethanol concentration revealed a linear correlation, further validating the precision and reliability of our experimental setup. Additionally, visual assessments of cuvettes containing ethanol−water mixtures provided a tangible representation of the spectroscopic data, substantiating our findings. The observed color shifts in conjunction with the acquired colorimetric responses further emphasize the accuracy and sensitivity of our constructed probe. Comparative assessments with commercially available Raman instruments, alongside the consistent performance demonstrated in our experiments, affirm that our custom-engineered instrument rivals its costly counterparts.

This achievement not only addresses the financial barriers associated with traditional Raman spectroscopy but also opens new possibilities for widespread applications, particularly in resource limited environments or educational settings. In

https://doi.org/10.1021/acsomega.4c04676
ACS Omega 2024, 9, 42822−42838

essence, our study not only presents a viable solution for affordable Raman spectroscopy but also showcases the potential of 3D printing technology in advancing scientific instrumentation. The success of this endeavor highlights the promising future of cost-effective and accessible analytical tools, ultimately contributing to the democratization of scientific research.

The future of the present work will focus on the limitations. The analysis of complex samples, such as biological tissues or multiphase materials, remains a formidable challenge requiring innovative strategies. Further refinement of quantitative analysis methods, enhancement of spatial resolution, and facilitation of in situ and real-time monitoring are ongoing research areas important for future research. Achieving cross-platform reproducibility remains a challenge, necessitating collaborative efforts for standardization. Further research should focus on the development of robust calibration models for complex mixtures and expanding the system's capabilities to handle a diverse range of samples. Exploring the adaptability of the system for portable and field applications is also a promising avenue. ML and DL techniques are increasingly applied to enhance Raman microscopy, offering advanced capabilities in spectral analysis and interpretation. These endeavors collectively contribute to overcoming existing challenges and shaping the future landscape of Raman spectroscopy-based research.

■ ASSOCIATED CONTENT

Data Availability Statement

The data underlying this study are available in the published article.

■ AUTHOR INFORMATION

Corresponding Authors

Ahmed Ali − *Department of Electrical Engineering, Sukkur IBA University, Sukkur 65200, Pakistan;* orcid.org/0000-0002-2645-7258; Email: ahmedali.shah@iba-suk.edu.pk

Kyung Min Byun − *Department of Biomedical Engineering and Department of Electronics and Information Convergence Engineering, Kyung Hee University, Yongin 17104, Republic of Korea;* orcid.org/0000-0001-8883-7072; Email: kmbyun@khu.ac.kr

Seung Ho Choi − *Department of Biomedical Engineering, Yonsei University, Wonju 26493, Republic of Korea; Department of Integrative Medicine, Major in Digital Healthcare, Yonsei University College of Medicine, Seoul 06229, Republic of Korea*; Phone: +82-33-760-2463; Email: seunghochoi@yonsei.ac.kr

Authors

Ezekiel Edward Nettey-Oppong − *Department of Biomedical Engineering, Yonsei University, Wonju 26493, Republic of Korea*

Jiwon Ahn − *Department of Biomedical Engineering, Yonsei University, Wonju 26493, Republic of Korea*

Riaz Muhammad − *Department of Biomedical Engineering, Yonsei University, Wonju 26493, Republic of Korea*

Hyun Jin Lee − *Department of Biomedical Engineering, Yonsei University, Wonju 26493, Republic of Korea*

Hyun-Woo Jeong − *Department of Biomedical Engineering, Eulji University, Seongnamsi 13135, Republic of Korea*

Complete contact information is available at: https://pubs.acs.org/10.1021/acsomega.4c04676

Author Contributions

[¶]E.E.N.-O. and A.A. authors contributed equally to this work. Conceptualization, S.H.C., A.A., E.E.N.-O., and H.J.L.; methodology, S.H.C., A.A., E.E.N.-O., and H.J.L.; formal analysis, S.H.C., A.A., E.E.N.-O., and H.J.L.; data curation, A.A., E.E.N.-O., and H.J.L.; writing—original draft preparation, A.A., and E.E.N.-O.; writing—review and editing, E.E.N.-O., A.A., M.R., and J.A.; visualization, A.A., E.E.N.-O.; and H.J.L.; supervision, S.H.C., A.A., H.W.J., and K.M.B.; project administration, S.H.C., A.A., H.W.J., and K.M.B.; funding acquisition, S.H.C. All authors have read and approved the final manuscript.

Notes

The authors declare no competing financial interest.

■ ACKNOWLEDGMENTS

This work was carried out with the support of "Research Program for Agriculture Science & Technology Development (project no. RS-2024-00399478)" Rural Development Administration, Republic of Korea. This work was also supported by the National Research Foundation of Korea (NRF), grant funded by the Korean government (MSIT) (nos 2022R1A2C1010151; 2022R1C1C1011328; 2022H1D3A2A02081592) and the Brain Korea 21 Four Program. This research was also supported by the MSIT (Ministry of Science and ICT), Korea, under the ITRC (Information Technology Research Center) support program (IITP-2024-RS-2024-00438239) supervised by the IITP (Institute for Information & Communications Technology Planning & Evaluation).

■ REFERENCES

(1) Chen, Y.; Hu, Y.; Li, G. A Review on Non-Noble Metal Substrates for Surface-Enhanced Raman Scattering Detection. *Chemosensors* **2023**, *11* (8), 427.

(2) Linh, V. T. N.; Ja'farawy, M. S. A.; Koh, E. H.; Lee, M.-Y.; Park, S.-G.; Kim, D.-H.; Jung, H. S. Flexible surface-enhanced Raman scattering substrates toward sampling approaches for on-site sensing and diagnosis applications. *Appl. Spectrosc. Rev.* **2023**, *59*, 90−123.

(3) Pahlow, S.; Richard-Lacroix, M.; Hornung, F.; Köse-Vogel, N.; Mayerhöfer, T. G.; Hniopek, J.; Ryabchykov, O.; Bocklitz, T.; Weber, K.; Ehricht, R.; et al. Simple, Fast and Convenient Magnetic Bead-Based Sample Preparation for Detecting Viruses via Raman-Spectroscopy. *Biosensors* **2023**, *13* (6), 594.

(4) Ali, A.; Nettey-Oppong, E. E.; Effah, E.; Yu, C. Y.; Muhammad, R.; Soomro, T. A.; Byun, K. M.; Choi, S. H. Miniaturized Raman instruments for SERS-based point-of-care testing on respiratory viruses. *Biosensors* **2022**, *12* (8), 590.

(5) Wilson, N. G.; Raveendran, J.; Docoslis, A. Portable identification of fentanyl analogues in drugs using surface-enhanced Raman scattering. *Sens. Actuators, B* **2021**, *330*, 129303.

(6) Safar, W.; Azziz, A.; Edely, M.; Lamy de la Chapelle, M. Conventional Raman, SERS and TERS Studies of DNA Compounds. *Chemosensors* **2023**, *11* (7), 399.

(7) Ali, A.; Hwang, E. Y.; Choo, J.; Lim, D. W. Nanoscale graphene oxide-induced metallic nanoparticle clustering for surface-enhanced Raman scattering-based IgG detection. *Sens. Actuators, B* **2018**, *255*, 183−192.

(8) Saraeva, I.; Zayarny, D.; Tolordava, E.; Nastulyavichus, A.; Khmelnitsky, R.; Khmelenin, D.; Shelygina, S.; Kudryashov, S. Locally Enhanced Electric Field Treatment of E. coli: TEM, FT-IR and Raman Spectrometry Study. *Chemosensors* **2023**, *11* (7), 361.

(9) Wells, K. L.; Alla, P. K.; Kaiser, K. G.; Murgulet, I. T.; Adragna, N. C.; Pavel, I. E. SERS of Human Red Blood Cells in Non-Resonant

Conditions: Benefits, Limitations, and Complementary Tools (CytoViva and GFAAS). *Chemosensors* **2023**, *11* (7), 353.
(10) Murugappan, S.; Tofail, S. A. M.; Thorat, N. D. Raman Spectroscopy: A Tool for Molecular Fingerprinting of Brain Cancer. *ACS Omega* **2023**, *8* (31), 27845−27861.
(11) Ren, P.; Zhou, R.-g.; Li, Y.; Xiong, S.; Han, B. Raman ConvMSANet: A High-Accuracy Neural Network for Raman Spectroscopy Blood and Semen Identification. *ACS Omega* **2023**, *8* (33), 30421−30431.
(12) Deidda, R.; Sacre, P.-Y.; Clavaud, M.; Coïc, L.; Avohou, H.; Hubert, P.; Ziemons, E. Vibrational spectroscopy in analysis of pharmaceuticals: Critical review of innovative portable and handheld NIR and Raman spectrophotometers. *TrAC, Trends Anal. Chem.* **2019**, *114*, 251−259.
(13) Shahbaz, M.; Tariq, A.; Majeed, M. I.; Nawaz, H.; Rashid, N.; Shehnaz, H.; Kainat, K.; Hajab, H.; Tahira, M.; Huda, N. u.; et al. Qualitative and Quantitative Analysis of Azithromycin as Solid Dosage by Raman Spectroscopy. *ACS Omega* **2023**, *8* (39), 36393−36400.
(14) Zhang, W.; Ma, J.; Sun, D.-W. Raman spectroscopic techniques for detecting structure and quality of frozen foods: principles and applications. *Crit. Rev. Food Sci. Nutr.* **2021**, *61* (16), 2623−2639.
(15) Ong, T. T.; Blanch, E. W.; Jones, O. A. Surface Enhanced Raman Spectroscopy in environmental analysis, monitoring and assessment. *Sci. Total Environ.* **2020**, *720*, 137601.
(16) Mojica, E.-R.; Dai, Z. New Raman spectroscopic methods' application in forensic science. *Talanta Open* **2022**, *6*, 100124.
(17) Lister, A. P.; Sellors, W. J.; Howle, C. R.; Mahajan, S. Raman scattering techniques for defense and security applications. *Anal. Chem.* **2021**, *93* (1), 417−429.
(18) Yang, Z.; Zhao, X.; Liu, J.; Wen, J.; Zhang, F.; Guo, X.; Zhang, K.; Zhang, J.; Wang, A.; Gao, R.; et al. Designed Growth of AgNP Arrays for Anti-counterfeiting Based on Surface-Enhanced Raman Spectroscopy Signals. *ACS Appl. Mater. Interfaces* **2022**, *14* (44), 50024−50032.
(19) Vandenabeele, P.; Edwards, H. G.; Moens, L. A decade of Raman spectroscopy in art and archaeology. *Chem. Rev.* **2007**, *107* (3), 675−686.
(20) Henry, D. G.; Jarvis, I.; Gillmore, G.; Stephenson, M. Raman spectroscopy as a tool to determine the thermal maturity of organic matter: Application to sedimentary, metamorphic and structural geology. *Earth-Sci. Rev.* **2019**, *198*, 102936.
(21) Culka, A.; Jehlička, J. A database of Raman spectra of precious gemstones and minerals used as cut gems obtained using portable sequentially shifted excitation Raman spectrometer. *J. Raman Spectrosc.* **2019**, *50* (2), 262−280.
(22) Bumbrah, G. S.; Sharma, R. M. Raman spectroscopy−Basic principle, instrumentation and selected applications for the characterization of drugs of abuse. *Egypt. J. Forensic Sci.* **2016**, *6* (3), 209−215.
(23) Lopez-Lopez, M.; Garcia-Ruiz, C. Infrared and Raman spectroscopy techniques applied to identification of explosives. *TrAC, Trends Anal. Chem.* **2014**, *54*, 36−44.
(24) Cialla-May, D.; Schmitt, M.; Popp, J. Theoretical principles of Raman spectroscopy. *Phys. Sci. Rev.* **2019**, *4* (6), 40.
(25) Volkmer, A. Vibrational imaging and microspectroscopies based on coherent anti-Stokes Raman scattering microscopy. *J. Phys. D: Appl. Phys.* **2005**, *38* (5), R59−R81.
(26) Larkin, P. *Infrared and Raman Spectroscopy: Principles and Spectral Interpretation*; Elsevier, 2017.
(27) Staveley, L. A. K. *The characterization of Chemical Purity: Organic Compounds*; Elsevier, 2016.
(28) Yaseen, M.; Cowsill, B. J.; Lu, J. R. 6-Characterisation of biomedical coatings. In *Coatings for Biomedical Applications*; Driver, M., Ed.; Woodhead Publishing, 2012; pp 176−220.
(29) Paarmann, L. D. *Design and Analysis of Analog Filters: A Signal Processing Perspective*; Springer Science & Business Media, 2006.
(30) Dhankhar, D.; Nagpal, A.; Rentzepis, P. M. Cell-phone camera Raman spectrometer. *Rev. Sci. Instrum.* **2021**, *92* (5), 054101.
(31) Bruker. SENTERRA II Raman Microscope. 2023, https://www.bruker.com/en/products-and-solutions/infrared-and-raman/raman-microscopes/senterra-ii-raman-microscope.html (accessed January 20, 2024).
(32) Johnson, D.; Larsen, P.; Fluellen, J.; Furton, D.; Schaertel, S. A. A Modular Raman Spectrometer for Solids. *Chem. Educ* **2008**, *13* (2), 82−86.
(33) Thermo Fisher Scientific. Thermo Scientific TruScan RM Next Generation Handheld Raman Analyzer. 2024, https://www.fishersci.com/shop/products/truscan-rm-next-generation-handheld-raman-analyzer/17375100#:~:text=Thermo%20Scientific%E2%84%A2%20TruScan%E2%84%A2%20RM%20Next%20Generation%20Handheld%20Raman,Catalog%20No.%2017-375-100%20%2486%2C500.00%20%2F%20Each%20of%201 (accessed January 20, 2024).
(34) Thorlabs. *Portable Coded-Aperture Raman Spectrometers*, 2024.
(35) Thermo Fisher Scientific. Thermo Scientific TruNarc Handheld Narcotics Analyzer. 2024, https://www.fishersci.com/shop/products/trunarc-handheld-narcotics-analyzer-6/p-7228743#?keyword=raman (accessed January 25, 2024).
(36) Thunder Optics. Eddu Raman System TO-ERS-532/TO-ERS-785. 2024, https://thunderoptics.fr/product/eddu-raman-system/ (accessed January 25, 2024).
(37) DeGraff, B. A.; Hennip, M.; Jones, J. M.; Salter, C.; Schaertel, S. A. An inexpensive laser Raman spectrometer based on CCD detection. *Chem. Educat.* **2002**, *7*, 15−18.
(38) Mohr, C.; Spencer, C. L.; Hippler, M. Inexpensive Raman spectrometer for undergraduate and graduate experiments and research. *J. Chem. Educ.* **2010**, *87* (3), 326−330.
(39) Young, M. A.; Stuart, D. A.; Lyandres, O.; Glucksberg, M. R.; Van Duyne, R. P. Surface-enhanced Raman spectroscopy with a laser pointer light source and miniature spectrometer. *Can. J. Chem.* **2004**, *82* (10), 1435−1441.
(40) Montoya R, E. H.; Baltuano-Elías, O.; Arbildo-López, A. A homemade cost effective Raman spectrometer with high performance. *J. Lab. Chem. Educ.* **2015**, *3*, 67.
(41) Aydogan, O.; Tasal, E. Designing and building a 3D printed low cost modular Raman spectrometer. *CERN IdeaSquare J. Exp. Innovat.* **2018**, *2* (2), 3−14.
(42) Somerville, W.; Le Ru, E.; Northcote, P.; Etchegoin, P. High performance Raman spectroscopy with simple optical components. *Am. J. Phys.* **2010**, *78* (7), 671−677.
(43) McCreery, R. L. *Raman Spectroscopy for Chemical Analysis*; John Wiley & Sons, 2005.
(44) Hickstein, D.; Goldfarmmuren, R.; Darrah, J.; Erickson, L.; Johnson, L. A Raman-spectroscopy-based sensor for rapid, accurate, and precise concentration measurements of a methanol-water mixture. **2018**, arXiv:1806.06404v1
(45) Meng, Z.; Cheng, S.; Petrov, G.; Jo, J.; Yakovlev, V. *Raman Spectroscopy Using Time-Correlated Photon-Counting Detection*; SPIE, 2013.
(46) PhysicsOpenLab. Raman Spectra of Alcoholic Molecules. 2023, https://physicsopenlab.org/2022/01/20/raman-spectra-of-alcoholic-molecules/ (accessed February 10, 2024).
(47) Huang, J.; Qin, Q.; Wang, J. A Review of Stereolithography: Processes and Systems. *Processes* **2020**, *8* (9), 1138.
(48) Kumar, M. B.; Sathiya, P.; Varatharajulu, M. Selective laser sintering. In *Advances in Additive Manufacturing Processes*; China Bentham Books: Beijing, China, 2021; p 28.

https://doi.org/10.1021/acsomega.4c04676
ACS Omega 2024, 9, 42822−42838